A method for unmixing magnetic hysteresis loops

David Heslop[1] and Andrew P. Roberts[1]

[1]   Hysteresis loops provide essential information concerning both induced and remanent magnetizations and are an important tool for characterizing magnetic mineral assemblages. Although the hysteresis behavior of mixed natural magnetic assemblages has been a focal point of much recent work, little progress has been made in unmixing of hysteresis loops into characteristic components. Unmixing strategies can act as cornerstones for interpretation of rock magnetic data and have become popular for characterizing isothermal remanent magnetization acquisition curves. Unmixing of hysteresis loops is, however, a challenging task because the individual component loops in the mixture must meet stringent shape constraints. We present a new technique for decomposing an ensemble of hysteresis loops into a small number of end-members based on linear mixing theory. The end-members are not based on type curves but instead are derived directly from the hysteresis data. Particular attention is paid to the form of the end-members, ensuring they meet the shape constraints expected for hysteresis loops of natural magnetic mineral assemblages. Marine sediments from the Southern Ocean and lake sediments from Butte Valley, northern California, provide case studies on which the proposed unmixing method is tested.

Citation: Heslop, D., and A. P. Roberts (2012), A method for unmixing magnetic hysteresis loops, *J. Geophys. Res.*, *117*, B03103, doi:10.1029/2011JB008859.

1.   Introduction

[2]   A large proportion of the magnetic mineral assemblages that occur in nature are composed of mixtures of minerals with different origins [cf. *Evans and Heller*, 2003]. To quantitatively analyze a given magnetic mineral assemblage and to draw inferences from its composition, it is necessary to identify and quantify its constituent magnetic components. The need for such quantification has been demonstrated over the last 30 years, with a strong focus being placed on decomposition of isothermal remanent magnetization (IRM) acquisition curves using a variety of approaches [*Thompson*, 1986; *Robertson and France*, 1994; *Stockhausen*, 1998; *Kruiver et al.*, 2001; *Heslop et al.*, 2002; *Egli*, 2003, 2004a, 2004b; *Heslop and Dillon*, 2007].
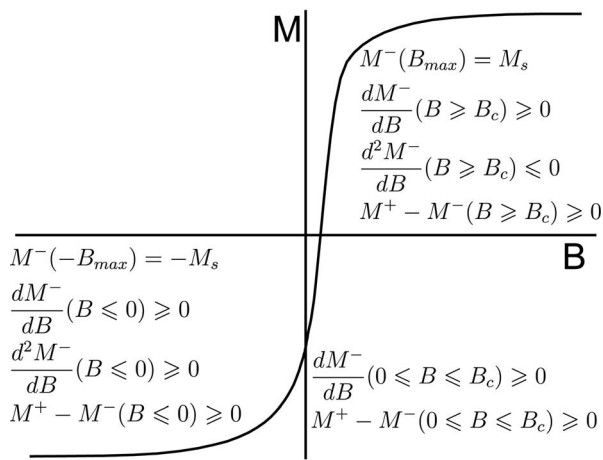
[3]   Hysteresis measurements play a key role in many rock and environmental magnetic investigations, and provide information concerning both the induced and remanent contributions to the magnetization. Compared to IRM acquisition curves, however, little attention has been given to the decomposition of hysteresis loops to quantify mixed magnetic mineral assemblages. A number of theoretical and experimental studies have employed forward modeling to investigate how magnetic mixtures are represented in hysteresis data with the aim of providing reference curves to which measured loops can be compared [*Roberts et al.*,

1995; *Tauxe et al.*, 1996; *Dunlop*, 2002; *Lanci and Kent*, 2003; *Heslop*, 2005; *Dunlop and Carter-Stiglitz*, 2006; *Carvallo et al.*, 2006]. Less focus, however, has been placed on the "unmixing" problem whereby hysteresis data are decomposed into meaningful components based only on the measured data and a number of theoretical/empirical assumptions [*von Dobeneck*, 1996; *Lascu et al.*, 2010].

[4]   Calculation of a solution that contains physically realistic components is the primary obstacle for unmixing hysteresis data. *Jackson and Solheid* [2010] outlined a number of shape properties that the majority of hysteresis loops can be expected to follow. These shape properties, which are expressed in terms of magnetization, M, as a function of applied field, B, are summarized in Figure 1 and play a key role in modeling hysteresis data.

[5]   Inspired by the work of *Rivas et al.* [1981], *von Dobeneck* [1996] proposed to fit the induced and remanent parts of a hysteresis loop using fictitious coercive particle classes based on hyperbolic basis functions. The advantage of such functions is their similarity in shape to the form of typical hysteresis loops. Thus, when mixed together in various combinations, hyperbolic functions should produce curves that meet the shape requirements for physically realistic hysteresis loops. *von Dobeneck* [1996] proposed that a library of hyperbolic basis functions should be generated and then numerical optimization can be employed to determine in what proportions the basis functions should be combined to provide a best fit to the experimental data. These proportions can then be represented as hyperbolic spectra for both the induced and remanent parts of the hysteresis loop to aid identification and quantification of

[1]Research School of Earth Sciences, Australian National University, Canberra ACT, Australia.

The diagram shows the M-B axes with the following annotations:

$M^-(B_{max}) = M_s$

$\dfrac{dM^-}{dB}(B \geqslant B_c) \geqslant 0$

$\dfrac{d^2M^-}{dB}(B \geqslant B_c) \leqslant 0$

$M^+ - M^-(B \geqslant B_c) \geqslant 0$

$M^-(-B_{max}) = -M_s$

$\dfrac{dM^-}{dB}(B \leqslant 0) \geqslant 0$

$\dfrac{d^2M^-}{dB}(B \leqslant 0) \geqslant 0$

$M^+ - M^-(B \leqslant 0) \geqslant 0$

$\dfrac{dM^-}{dB}(0 \leqslant B \leqslant B_c) \geqslant 0$

$M^+ - M^-(0 \leqslant B \leqslant B_c) \geqslant 0$

Figure 1. Example of the mathematical properties that physically realistic hysteresis loops should meet. This case is given in terms of a lower hysteresis branch, M^- (black curve) measured from the maximum negative field, $-B_{max}$, to the maximum positive field, B_{max}. Rewriting the properties in terms of an upper branch, M^+, is trivial as a result of the $M(B) = -M(-B)$ inversion symmetry expected for the hysteresis loops of geological materials. The properties of the first, third and fourth quadrants are presented. A monotonic change in magnetization is expected throughout M^-. The lower (upper) branch will be concave up (concave down) for fields in the interval $[-B_{max}, 0]$ and concave down (concave up) in the interval $[B_c, B_{max}]$, where B_c denotes the coercive force. Within the interval $[0, B_c]$, the branch may contain one or more inflection points. Finally, the upper and lower branches should never cross, which can be represented by the property; $M^+ - M^- \geq 0$.

discrete mineral or domain state fractions. *Jackson and Solheid* [2010] subsequently showed that not all hysteresis loops follow a form that can be approximated by hyperbolic functions, for example, those that contain multiple inflections. To provide a more flexible library of basis curves, *Jackson and Solheid* [2010] proposed the use of sigmoid logistic functions that are offset horizontally and vertically to produce double-logistic curves.

[6] The principal limitation of fitting libraries of basis curves to a measured hysteresis loop is that the problem is extremely ill-conditioned, which arises from the strong correlation that exists amongst the basis curves. This means that the regression problem suffers from multicollinearity; small changes in the data can therefore lead to large changes in the estimated mixing coefficients [*Marques de Sá*, 2007]. Multicollinearity is not an issue if the aim of the fitting procedure is to simply obtain a smoothed approximation to a measured loop (à la *Jackson and Solheid* [2010]). It is, however, a serious problem if the mixing coefficients are to be interpreted to draw inferences concerning the composition of the magnetic mineral assemblage in terms of discrete components.

[7] Previous unmixing methods applied to IRM acquisition curves have focused on decomposing the data using collections of parametric functions [*Robertson and France*, 1994; *Kruiver et al.*, 2001; *Heslop et al.*, 2002; *Egli*, 2003, 2004a, 2004b]. More recently, *Heslop and Dillon* [2007]

employed an "end-member" unmixing strategy designed to provide a genetically meaningful decomposition of IRM acquisition data by separating suites of curves into collections of invariant parts. Such an unmixing is based on examination of the covariation of behavior across a collection of samples to define a mixing space empirically and thus focuses on the processes that control the magnetic mineral assemblage. In this way, there is no requirement for an individual end-member to be composed of a single mineral or domain state. Instead, it will most likely correspond to a mixture of different minerals and/or domain states that originate from a common and compositionally invariant source.

[8] We present here an unmixing method that is based on estimation of end-members from collections of hysteresis loops. In this way, there is no reliance on construction of a set of appropriate basis functions and the problem is not influenced by multicollinearity. The proposed unmixing strategy involves decomposition of a suite of hysteresis loops into a small number of invariant hysteresis loops that are considered to be end-members. When mixed together in specific proportions, these end-members should recreate the original hysteresis data set. The components can be interpreted as being representative of the underlying processes that control the magnetic mineral assemblage in the studied samples. The determined mixing coefficients provide a framework for quantitative interpretation of the hysteresis loops in terms of processes that gave rise to the mixed magnetic mineral assemblage. The general unmixing problem and its possible solutions are described below with particular attention on detailed model selection to recover end-members that represent physically realistic hysteresis loops. Two case studies are provided to demonstrate the proposed method. In the first, we investigate marine sediments from the Southern Ocean [*Roberts et al.*, 2011a] and demonstrate how hysteresis unmixing can provide information to aid design of more detailed experimental investigations. In the second case study, hysteresis data are examined for lake sediments from Butte Valley, northern California [*Roberts et al.*, 1996]; we show how a hysteresis unmixing model can provide quantitative information to supplement environmental interpretations.

2. Formulation of the Mixing Model

[9] To construct the unmixing problem, we assume that an ensemble of n measured hysteresis loops is composed of a linear combination of p end-member loops, where $p \ll n$. To ensure meaningful comparison, the hysteresis loops must have been measured using the same field steps and averaging times. Additionally, in the case of assemblages with paramagnetic/diamagnetic contributions or those with an extended approach to saturation [*Fabian*, 2006], the loops must have been measured to the same maximum field (B_{max}) to ensure consistent high-field correction. A robust mixing model requires high-quality data sets with measured loops that close at high fields and that have high signal-to-noise ratios. Measured loops should be adjusted for both vertical and horizontal offsets by finding their centers of symmetry and where necessary the loops should be corrected for drift (these data preparation operations can be performed using the approaches outlined by *Jackson and Solheid* [2010]).
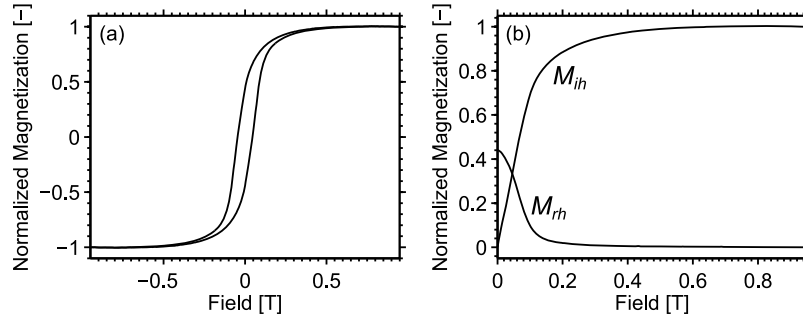
Figure 2. (a) An example of a measured hysteresis loop. (b) The remanent hysteretic and induced hysteretic magnetization curves for example loop in Figure 2a calculated via equations (1)–(4).

Once the loops are centered and drift corrected, any paramagnetic/diamagnetic contributions can be removed by estimation of the linear high-field slope, or alternatively, where necessary a nonlinear approach to saturation correction can be made [*Fabian*, 2006; *Jackson and Solheid*, 2010]. Finally, the corrected loops must be normalized so that their maximum magnetization, $\hat{M}$, is unity. It is important to note that when high-coercivity minerals are present, which do not saturate in typical laboratory fields, $\hat{M}$ will underestimate the true saturation magnetization, M_s. This also has important implications for the final unmixing model because high-coercivity minerals that are not saturated fully during hysteresis measurement will be underrepresented.

[10] Under the assumption that hysteresis loops for geological materials exhibit inversion symmetry [*Jackson and Solheid*, 2010], the upper $M^+(B)$ and lower $M^-(B)$ branches of a corrected and normalized loop can be used to estimate the induced hysteretic, M_{ih}, and remanent hysteretic, M_{rh}, curves [*Rivas et al.*, 1981]:

$$M_{ih}(B) = (M^+(B) + M^-(B))/2, \tag{1}$$

$$M_{rh}(B) = (M^+(B) - M^-(B))/2. \tag{2}$$

M_{ih} should exhibit inversion symmetry through the origin and M_{rh} should have reflection symmetry about the M axis. Therefore, the two sides of the M_{ih} and M_{rh} curves can be averaged to help remove measurement noise:

$$M_{ih}(|B|) = (M_{ih}(B) - M_{ih}(-B))/2, \tag{3}$$

$$M_{rh}(|B|) = (M_{rh}(B) + M_{rh}(-B))/2. \tag{4}$$

An example of this procedure is given in Figure 2. The final data are placed in a matrix $X = [\boldsymbol{M_{ih}}(B \geq 0) \boldsymbol{M_{rh}}(B \geq 0)]$, which is composed of n rows (1 per sample) and l columns (1 per field for the M_{ih} and M_{rh} inputs). The M_{ih} and M_{rh} curves that represent the end-members are stored in a $p \times l$ matrix, $\boldsymbol{S}$, and the fractional abundances of each of the end-members in each of the samples are held in a $n \times p$ matrix, $\boldsymbol{A}$. The linear mixing system is then given in matrix notation by

$$X = AS + E \quad \text{subject to } A \geq 0, A\boldsymbol{1_p} = 1, \tag{5}$$

where $\boldsymbol{1_p}$ is a column vector of length p composed of ones and $\boldsymbol{E}$ is a $n \times p$ matrix of errors (the difference between the model and data). The $\boldsymbol{A} \geq 0$ constraint ensures that the relative abundances are nonnegative and, hence, are physically meaningful. Additionally, each row of $\boldsymbol{A}$ must sum to unity (enforced by the $\boldsymbol{A1_p} = 1$ constraint), which given that the hysteresis data have been normalized to $\hat{M}$, ensures conservative mixing. The end-member hysteresis loops can be obtained by separating the matrix $\boldsymbol{S}$ into its induced and remanent hysteretic parts and reversing the procedure outlined in equations (1)–(4). Additionally, the remanent hysteretic parts of the end-members can be compared directly to the magnetic components retrieved from analysis of remanent magnetization curves [*Robertson and France*, 1994; *Stockhausen*, 1998; *Kruiver et al.*, 2001; *Heslop et al.*, 2002; *Egli*, 2003, 2004a, 2004b].

2.1. Estimating the Optimal Mixing Model

[11] Solution of the mixing problem involves estimating both $\boldsymbol{A}$ and $\boldsymbol{S}$ from $\boldsymbol{X}$. This is a nonlinear problem and a unique solution to equation (5) cannot exist. Consideration of the geometry of the problem, however, indicates how a realistic solution to equation (5) can be obtained. If the end-member loops are linearly independent and linear additivity holds [*Roberts et al.*, 1995; *Lees*, 1997; *Carter-Stiglitz et al.*, 2001; *Carvallo et al.*, 2006], the observations in $\boldsymbol{X}$ will lie within a $p - 1$ dimensional simplex defined by $\boldsymbol{S}$, with the end-member compositions given by the positions of the vertices of the simplex. A $p - 1$ dimensional simplex of any size and orientation would satisfy the constraints in equation (5) providing that it bounds all cases in $\boldsymbol{X}$. This demonstrates the nonunique nature of the unmixing problem. To find the most geologically feasible solution to equation (5) on the basis of the data, it is necessary to find the smallest volume $p - 1$ dimensional simplex that bounds all observations (Figure 3a). Using this approach, the end-members will be close to the cases in $\boldsymbol{X}$ and should therefore be characterized by geologically realistic compositions [*Ehrlich and Full*, 1987; *Craig*, 1994; *Renner*, 1995; *Weltje*, 1997]. One limitation of this approach, however, is that the determined end-members may be combinations of the true end-members if the natural system only produces a limited range of mixtures. This concept is demonstrated graphically for a three end-member system in Figure 3b. Under such circumstances, an attempt to recover the pure end-members would require extrapolation of the mixing space into regions with no data coverage. Given the nonunique nature of the unmixing problem, such an extrapolation is not
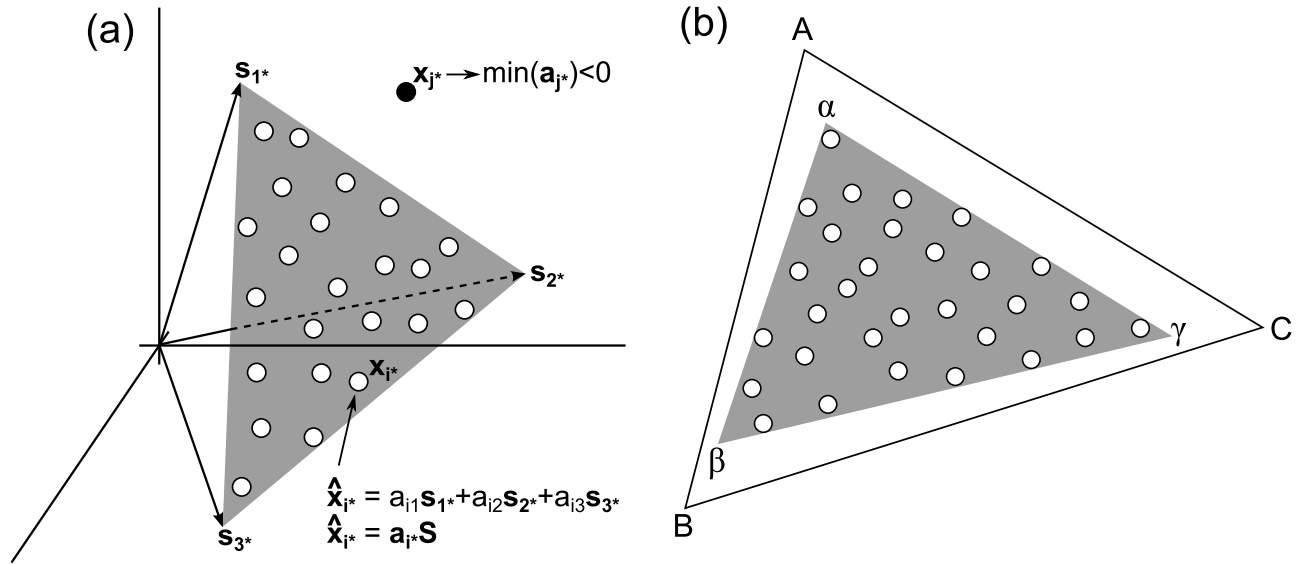
Figure 3. (a) Schematic diagram of the construction of a three end-member unmixing model. For a p end-member model, each hysteresis loop in X should be representable as a single point in p-dimensional space (marked as circles in the $p = 3$ example). The best fit model to the data is the smallest $p - 1$ dimensional simplex that bounds all of the data points (the gray triangle). The vertices of the simplex defined by the rows of S correspond to the end-member loops in p-dimensional space. Loops, such as x_{i*}, that lie within the simplex meet the constraints of equation (5), with the values of a_{i*} being nonnegative and summing to unity. The equation (given with its equivalent form in matrix notation) indicates how a prediction of x_{i*}, denoted as $\hat{x}_{i*}$, can be calculated from the end-member mixing model using both A and S. Loop x_{j*} lies outside of the mixing space defined by the simplex. Its distance from the other points indicates that it may potentially be an outlier. For such nonbounded cases, one or more of the values in a_{j*} will be negative and the constraints of equation (5) are not met. (b) Illustration of the mixing space (gray shading) defined by the data (circles) compared to the true end-members of the mixing system (A, B and C on the black triangle). Consider the mixing space bounded by the black line which consists of the three natural end-members, A, B and C. The natural mixing system is limited in the combinations of the end-members it produces so that the available samples (circles) only reside within a restricted region of the mixing space and do not extend to its boundaries. The unmixing algorithm attempts to find the smallest simplex (shaded region) that will bound the measured data points. The empirical end-members are given by the vertices of the fitted simplex, which are denoted by the positions of α, β and γ, which means they themselves represent mixtures of A, B and C.

employed here. Any such attempts should be based on a detailed understanding of the rock magnetism of a sample set under consideration.

[12] Several algorithms have been developed to find the minimum volume simplex that bounds a collection of points in high-dimensional space [*Craig*, 1994; *Miao and Qi*, 2007; *Chan et al.*, 2009]. We use the simplex identification via split augmented Lagrangian (SISAL) algorithm of *Bioucas-Dias* [2009], which has the advantage of being robust to outliers. Robustness is achieved by making the non-negativity of A a soft, rather than a hard, constraint. If a case in X lies outside the simplex defined by S, then one or more of its corresponding values in A will be negative (Figure 3a). The SISAL algorithm penalizes negative components of A proportionally to their magnitude according to a regularization parameter λ which must be greater than 0. As λ is decreased, the simplex defined by S becomes smaller as more cases in X are allowed to reside outside the simplex. Thus, appropriate selection of λ makes S resistant to outliers and to large noise contributions. A strategy for selecting an appropriate value of λ is given below.

2.2. End-Member Constraints

[13] One key aspect for the final determination of S is that the positions of the vertices correspond to hysteresis loops that obey the shape constraints outlined in Figure 1. These shape properties could be included in the determination of S as a collection of nonlinear inequality and equality constraints. Numerical experiments indicate, however, that such an approach suffers from large numbers of local minima in which optimization routines become trapped. As an alternative approach, the SISAL algorithm is employed according to equation (5) . Then, after convergence is reached, the end-members in S are examined to assess if they are close to meeting the shape constraints shown in Figure 1. This assessment provides an important model selection criterion. Physically unrealistic end-members may be indicative of an under or overly complex model (i.e., incorrect selection of p), an inappropriate value of λ or more fundamentally that the samples do not originate from a mixing system or that they do not obey the assumptions of the model (i.e., linear additivity).
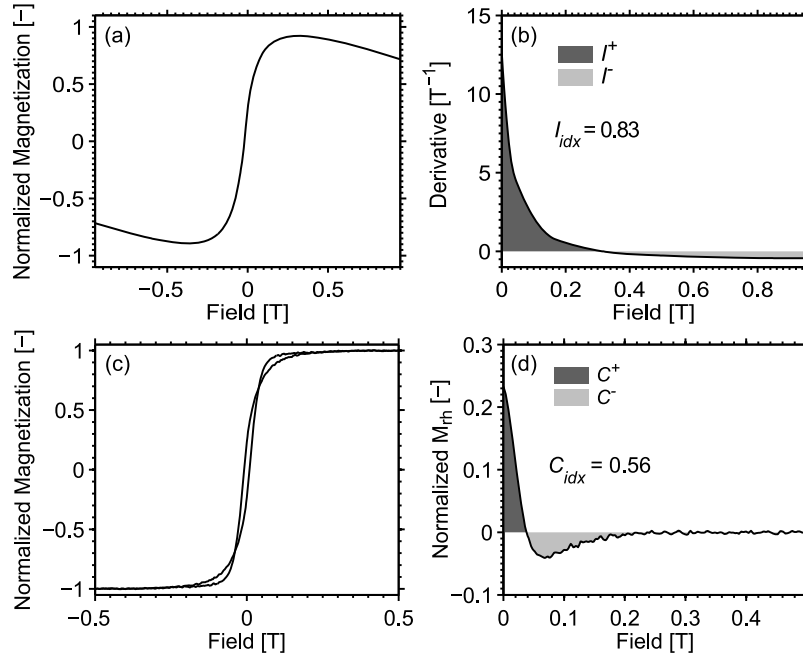
Figure 4. (a) An example of an upper hysteresis branch that does not exhibit monotonic behavior. (b) For positive fields the regions of the branch with positive (dark shading) and negative (light shading) derivatives can be compared to quantify the overall monotonicity of the branch in the form of the metric I_{idx}. (c) An example of a hysteresis loop with crossovers between its upper and lower branches. (d) The associated M_{rh} curve has negative values when the crossover constraint is violated. Therefore, a comparison of the regions of the M_{rh} curve above (dark shading) and below (light shading) zero can be used to quantify the extent of crossovers and form the basis of the C_{idx} metric.

[14] We propose two metrics to assess the monotonicity, $dM/dB \geq 0$, and noncrossing, $M^+(B) - M^-(B) \geq 0$, constraints for hysteresis loops. The monotonicity metric is calculated by fitting a piecewise cubic Hermite interpolating polynomial to the upper branch of a given end-member loop (the end-member loops have inversion symmetry so it is not necessary to consider the lower branch). The polynomial, $\hat{f}$, is shape preserving and is not affected by the oscillations often associated with cubic splines [*Kahaner et al.*, 1989]. The field values at which the derivative of the fitted polynomial crosses zero, i.e., $\hat{f}'(B) = 0$, can be found directly from its coefficients. The regions of $\hat{f}$ between the zero-crossing points define intervals in which $\hat{f}$ is monotonic. To assess the overall monotonicity of $\hat{f}$, the integral of $\hat{f}'$ is found for each monotone interval (note, because the M_{ih} curve exhibits inversion symmetry it is only necessary to consider $B \geq 0$). For example, if x and y represent adjacent zero-crossing points:

$$I = \int_x^y \hat{f}'(B)dB. \tag{6}$$

The increasing intervals (I^+) and decreasing intervals (I^-) of $\hat{f}$ are summed separately and are formed into the ratio:

$$I_{idx} = \frac{\sum I^+}{\sum I^+ + \sum |I^-|}. \tag{7}$$

For a monotonically increasing (decreasing) magnetization with respect to the applied field, I_{idx} will yield a value of 1(0).

An example of this approach is given in Figure 4, where a numerically constructed loop with clear nonmonotonic behavior is examined. Values of I_{idx} are expected to be generally high because $\hat{f}(0) = 0$ and $\hat{f}(B_{max}) = 1$ are fixed points resulting from the unmixing. Therefore, end-members must show a generally increasing trend with respect to B. For natural samples, measurement noise in the high-field portions of loops may reduce I_{idx} slightly. This is especially the case for loops that close at low fields and that have been corrected for paramagnetic/diamagnetic contributions and are thus flat at high fields.

[15] Calculation of the crossover metric follows a similar concept to the monotonicity metric. When represented in the form of M_{ih} and M_{rh} curves, a hysteresis loop will exhibit a crossing of the upper and lower branches when $M_{rh} \leqslant 0$. A piecewise cubic Hermite interpolating polynomial is fitted to the $M_{rh}(B \geq 0)$ curve of a given end-member and is examined for zero crossings that mark the fields at which the branches M^+ and M^- cross (the M_{rh} curve exhibits reflection symmetry about the magnetization axis, therefore it is not necessary to consider $M_{rh}(B < 0)$). In a manner similar to the monotonicity metric, the positive and negative regions of the fitted polynomial, $\hat{f}$, are integrated separately and are summed according to their sign to give C^+ and C^-, respectively. These values are then compared to give the crossover index:

$$C_{idx} = \frac{\sum C^+}{\sum C^+ + \sum |C^-|}. \tag{8}$$

A value of $C_{idx} = 1$ indicates that there is no crossover between M^+ and M^-. $C_{idx} \to 0$ as the extent of crossover increases. Acceptable values of C_{idx} depend on the form of the loop being examined. In the case of high-coercivity assemblages, which do not saturate in B_{max}, M_{rh} should be greater than 0 at all positive fields except B_{max}. Therefore even small crossovers at lower fields may be indicative of a problem with the end-member loop. In contrast, super-paramagnetic (SP) particles should yield $M_{rh} = 0$ for all fields, in which case small fluctuations can cause large numbers of small crossovers that will reduce C_{idx} while the loop remains effectively realistic. An example of C_{idx} is given in Figure 4 where a numerically constructed loop containing large crossovers is examined. Natural samples that reach saturation during measurement are not expected to yield $C_{idx} = 1$ because crossovers may occur as a result of measurement noise in the high-field portion of the loop once the branches are closed. These crossovers are expected, however, to be minor and therefore C_{idx} should be close to 1.

[16] As discussed above, the I_{idx} and C_{idx} values associated with acceptable end-members will change depending on the form of the given end-member loop. For this reason we see the primary role of I_{idx} and C_{idx} as metrics to compare a p end-member model with a more complex $p + 1$ model rather than parameters with which loops can be deemed to be unequivocally physically realistic.

2.3. Model Complexity and Selection of λ

[17] Model selection in terms of the number of end-members to be included in the decomposition of X is a challenging task. If the model does not contain enough end-members it will not provide a good fit to the measured loops and the data may not be decomposed sufficiently to allow clear interpretation in terms of separate processes. Alternatively, if too many end-members are included the mixing model will be overly complex, which will inhibit interpretation and render the unmixing model ineffective as a tool with which to understand the hysteresis data set. To guide model selection, we adopt the principle of parsimony as proposed by *Imbrie* [1963] for the specific case of unmixing models. *Imbrie* [1963] recommended that the simplest model (i.e., the one with the minimum number of end-members) that provides a good fit to the data and that can be interpreted in a geologically meaningful way should be deemed to be the most appropriate.

[18] Initial model selection is guided by eigenvector-based analysis of the data [*Ehrlich and Full*, 1987]. A collection of samples generated by a perfect linear mixing system comprising p end-members can be described completely by the first $p - 1$ eigenvectors of the data set. Principal component analysis can therefore act as a guide to model selection by providing an estimate of the proportion of the data variance that will be accounted for by p end-members (i.e., the data variance that is accounted for by the first $p - 1$ principal components).

[19] Selection of an appropriate value of λ (which controls the size of the fitted simplex) is also key to construction of a meaningful mixing model. To estimate the optimal value of λ for a given data set we adopt a bootstrap approach combined with the introduced I_{idx} and C_{idx} metrics. A single bootstrap iteration is performed by selecting n rows from the data matrix, X, to form a new input matrix; X^{boot}. This

procedure is performed *with replacement*, thus it is possible for any given row of X to appear in X^{boot} more than once. The mixing model described by equation (5) is then estimated for predefined values of p and λ to yield A^{boot} and S^{boot}. On the basis of S^{boot}, A can be estimated for X and a convexity error of the solution determined (Appendix A). The metrics I_{idx} and C_{idx} can then be calculated for the end-members in S^{boot}. The above procedure can be repeated for a large number of iterations, typically of the order 10^3, for fixed values of p and λ to generate distributions of I_{idx} and C_{idx} and the convexity error. For a given p the aim is to find a value of λ that yields a simplex large enough to bound as many of the observations in X as possible (indicated by a low convexity error) while maintaining physically realistic end-members as indicated by values of I_{idx} and C_{idx} close to 1.

3. Case Study 1: Southern Ocean Sediments

[20] A collection of 38 hysteresis loops, measured to a maximum field of 0.5 T, from Ocean Drilling Program (ODP) Holes 689D, 690C, 738B and 738C were amalgamated into a single data set. ODP Sites 689 and 690 are situated on Maud Rise in locations estimated to have had paleowater depths of $\sim$1600 m and $\sim$2400 m, respectively [*Kennett and Barker*, 1990]. The analyzed Maud Rise sediments are pelagic carbonates of Oligocene age (four samples from Hole 689D and seven samples from Hole 690C). ODP Site 738 is located on the southern Kerguelen Plateau with an estimated paleowater depth of $\sim$1750 m. Pelagic carbonate samples were taken from Holes 738B (n = 12) and 738C (n = 15) through the Eocene and the Paleocene–Eocene Thermal Maximum (PETM) intervals, respectively [*Barron et al.*, 1991].

[21] The measured hysteresis loops have a high signal-to-noise ratio with a mean Q value of 4.7 [cf. *Jackson and Solheid* 2010]. The loops were processed using the method discussed in section 2 and formed into the data matrix, X. The first 2 principal components of X explain $\sim$94% of the data variability, while the first 3 principal components explain $\sim$97%. This suggests that a 3 end-member model will perform well in forming a mixing model for the data, while addition of a fourth component will provide only a small improvement. A more detailed model selection procedure to determine optimal values of p and λ was made using the bootstrap approach outlined above.

[22] For a given value of λ, a three end-member model was calculated using 10^3 bootstrap iterations. For each iteration, I_{idx} and C_{idx} were calculated for the returned end-members. The median values of I_{idx} and C_{idx} for each value of λ provide useful indicators for model selection (Figure 5). As expected the three end-member model has improved convexity error (i.e., samples are being bound by, or are becoming closer to, the mixing simplex) as λ increases. Simultaneously, however, the quality of the end-members gradually degrades as λ increases and the vertices of the simplex enter regions that do not correspond to physically realistic hysteresis loops. In particular, I_{idx} becomes low for higher values of λ, but such values could still be attributed to the effects of noise that cause small fluctuations in the monotonicity of the end-members. Once λ passes a value of $\sim$2, little improvement is seen in the
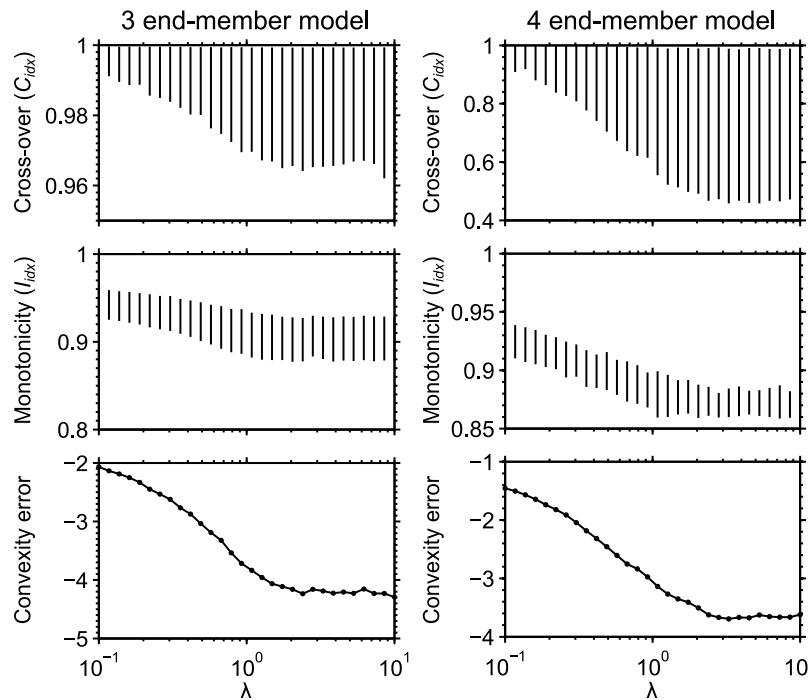
Figure 5. Model selection statistics for (left) three and (right) four end-member unmixing of the analyzed Southern Ocean sediment hysteresis loops. Each line represents the span of the medians of a given parameter for the end-members obtained from 10^3 bootstrap iterations. As λ increases, the convexity error improves but at the cost of a slight degradation in the form of the end-members (i.e., reduced monotonicity and an increase in crossovers). For $p = 3$, a value of $\lambda = 2$ is selected because the end-members have acceptable forms, and for high values of λ there is no improvement in the convexity error. For $p = 4$, low values of C_{idx} indicate that one or more end-members contain large crossovers even at low values of λ. This suggests that a low convexity error four end-member mixing model cannot be constructed with physically realistic end-members. A three end-member mixing model is therefore more physically realistic for these data.

convexity error while the quality of the loops continues to degrade slowly. Therefore, $\lambda = 2$ appears to be a suitable choice for a three end-member model in the case of the studied Southern Ocean sediments.

[23] When the selection procedure is repeated for a four end-member model (Figure 5) one of the end-members yields a high crossover index even at values of λ that yield unacceptable convexity errors (i.e., many samples are still not bound by the mixing simplex). The convexity error improves as λ increases but the low values of C_{idx} indicate that the unmixing is producing a physically unrealistic end-member. This comparison of the three and four end-member solutions demonstrates that a three end-member model is more successful at bounding the samples while maintaining end-members that are physically realistic. Allied with the principal of parsimony [*Imbrie*, 1963], this observation leads us to select a three end-member model with $\lambda = 2$ for the final mixing model.

[24] The final end-member loops (Figure 6) were determined by averaging 10^3 bootstraps with a median convexity error of approximately -4.2. The large-scale structures of the end-member loops obey the shape constraints outlined in Figure 1, and they appear to be physically realistic. The form of the end-member hysteresis loops and independent information concerning the magnetic mineral assemblages at the

investigated ODP sites facilitates characterization of the end-members.

[25] End-member 1 has a form typical of pseudosingle domain (PSD) to multidomain (MD) magnetite and is consistent with the PSD magnetite and/or low-Ti titanomagnetite identified as a major remanence carrier at ODP Sites 689, 690 and 738 [*Florindo and Roberts*, 2005; *Roberts et al.*, 2011a]. The larger grain size of end-member 1 suggests that it corresponds to a detrital magnetic component. End-member 2 is characteristic of single domain (SD) material and given the environmental setting can be attributed to magnetofossils produced by magnetotactic bacteria [cf. *Egli* 2004a]. *Roberts et al.* [2011a] reported the consistent presence of a biogenic magnetite component throughout the Eocene sediments of ODP Hole 738B and argued that it is responsible for the stable palaeomagnetic signal at 738B. Finally, the hysteresis loop for end-member 3 remains open at higher fields, which indicates the possible presence of a high-coercivity contribution. End-member 3 probably corresponds to eolian material that is enriched in hematite [cf. *Roberts et al.*, 2011a].

[26] The mean relative contributions of the end-members to each of the studied sample sets are shown in Figure 6. ODP Site 689 is somewhat richer in magnetofossils (end-member 2) compared to neighboring Site 690, while the relative abundance of detrital magnetite (end-member 1) is
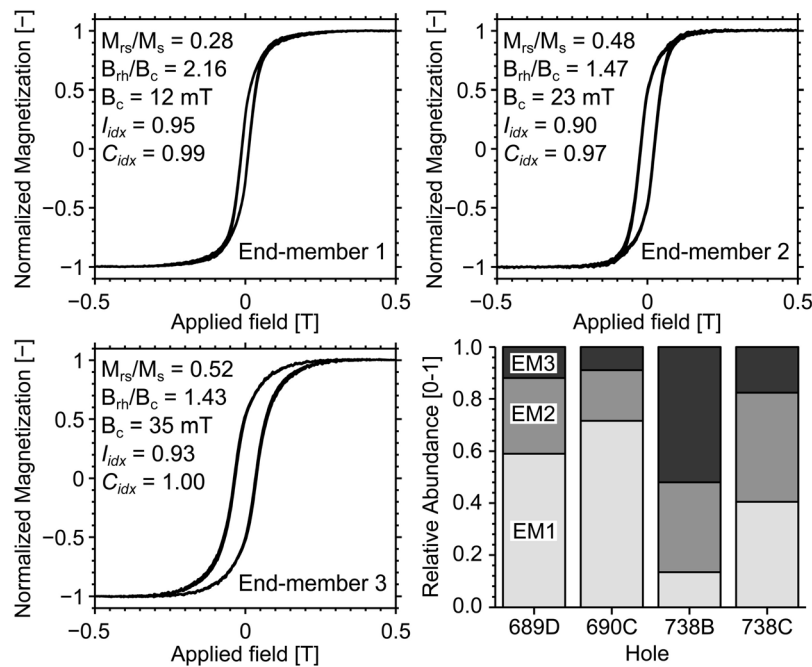
Figure 6. The three end-members obtained from the combined mixing model from ODP Sites (top left) 689, (top right) 690 and (bottom left) 738. Each loop is shown as a shaded region indicating the mean loop ±1 standard error (estimated from the bootstrap procedure). For each loop, the coercivity (B_c) and the ratios of the saturation remanent magnetization to the saturation magnetization (M_{rs}/M_s) and the median field of the remanent component of the loop to the coercivity (B_{rh}/B_c) are shown [*Fabian and von Dobeneck*, 1997]. Additionally, the monotonicity index, I_{idx}, and crossover index, C_{idx}, are given. (bottom right) Mean relative abundances of the three end-members for each of the studied ODP holes. The total data set is composed of 38 hysteresis loops, comprising 4, 7, 12 and 15 samples from ODP Holes 689D, 690C, 738B and 738C, respectively.

lower compared to site 690. This comparison is based on a small number of samples and slight differences in the compositions must be treated with caution. It is possible, however, that differences in the magnetic mineral assemblages can be attributed to the different locations and water depths of the two sites. For example, during the Oligocene, Site 690 is thought to have been bathed in cold Antarctic Bottom Water, while Site 689 was not [*Diester-Haass*, 1991]. Earlier studies have shown that magnetofossil abundance at a given location is, at least partially, a function of environmental conditions and thus the differences at the two sites may be a result of them sitting in different water masses [*Hesse*, 1994] and possibly experiencing different nutrient conditions [*Roberts et al.*, 2011a]. In terms of terrigenous inputs, the differences between Sites 689 and 690 might result from the relative importance of supply from different sources. Alternatively, the relative contributions of end-members 1 and 3 are only slightly different at Sites 689 and 690 and might result from local processes such as winnowing that occurred to a greater extent at Site 689 [*Diester-Haass*, 1991].

[27] The primary difference between Holes 738B and 738C is the composition of the detrital component, which is magnetite rich in the case of Hole 738C and hematite rich in the case of Hole 738B. Given the ~20 Myr age difference between the Hole 738B (Eocene) and Hole 738C (PETM) sediments, the differences in terrigenous input could have a number of causes. *Roberts et al.* [2011a] showed that the eolian flux at Hole 738B increased gradually from relatively low levels during the late Eocene. This eolian component contained a hematite contribution, which accounts for the high relative abundance of end-member 3 at Hole 738B. In contrast, the PETM was a time when the global hydrological cycle was enhanced [*Bowen et al.*, 2004; *Pagani et al.*, 2006; *Harding et al.*, 2011], making it possible that the relatively larger detrital magnetite component (end-member 1) at Hole 738C resulted from lower levels of oxidation in the sediment source areas.

[28] In this example, our proposed hysteresis unmixing approach can be employed to provide information to aid design of future studies. On the basis of the unmixing results the presence of two terrigenous components and a biological component is hypothesized. Testing this hypothesis would require more detailed investigations, which would be facilitated by the unmixing results.

4. Case Study 2: Plio-Pleistocene Lake Sediments

[29] Plio-Pleistocene fine-grained lake sediment samples from Butte Valley, northern California, were examined as part of a number of rock magnetic studies [*Roberts et al.*, 1995, 1996, 2000; *Pike et al.*, 2001]. These investigations reveal a complex magnetic mineralogy, which provides an example to demonstrate the proposed hysteresis unmixing approach.

[30] The Butte Valley catchment is part of the larger Klamath basin, and includes basalts and basaltic andesites
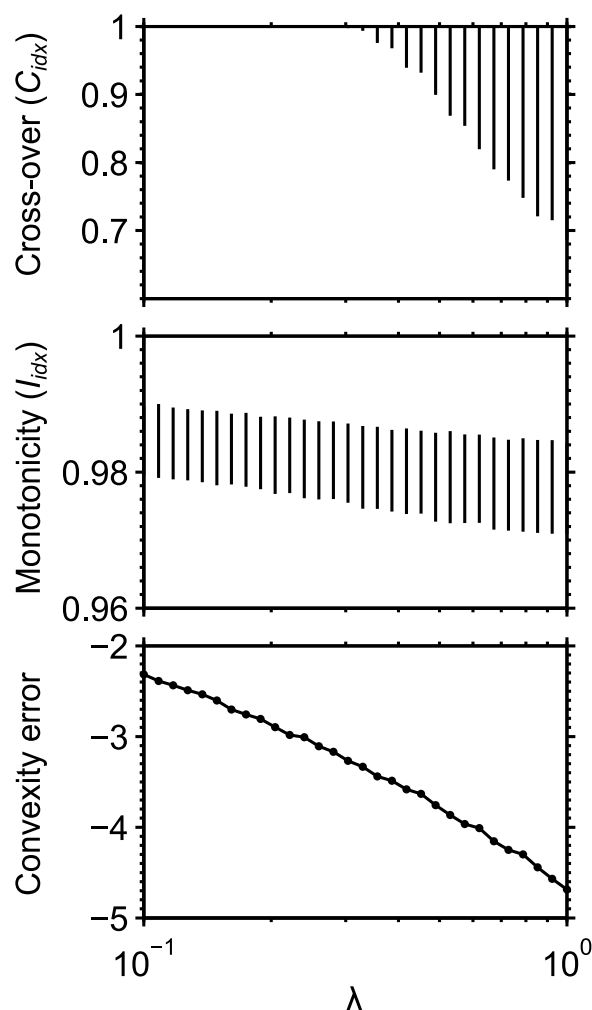
Figure 7. Model selection statistics for a three end-member unmixing of the Butte Valley hysteresis loops. Each line represents the span of the medians of a given parameter for the end-members obtained from 10^3 bootstrap iterations. There is a clear break at $\lambda \approx 0.33$ when one of the end-members starts to develop branches that cross (indicated by a lowering of C_{idx}).

that have been eroded to provide titanomagnetite within the detrital magnetic component of the lake sediments [*Roberts et al.*, 1996]. X-ray diffractograms from magnetic mineral extracts and optical microscopy of the extracts reveal the presence of hematite in the sediments, which has also been assumed to be detrital in origin [*Roberts et al.*, 1996]. The existence of high concentrations of SD particles in some stratigraphic intervals has been demonstrated by elevated values of the ratio of saturation remanent magnetization to the mass-dependent magnetic susceptibility (M_{rs}/χ) [*Roberts et al.*, 1996] and by first-order reversal curve (FORC) diagrams [*Roberts et al.*, 2000]. On the basis of X-ray diffractograms of magnetic extracts these SD particles have been demonstrated to be authigenic greigite [*Roberts et al.*, 1996]. Finally, wasp-waisted hysteresis loops, low-temperature measurements, high-frequency-dependent magnetic susceptibilities and FORC diagrams have been used to demonstrate the presence of a substantial SP component in

many Butte Valley samples [*Roberts et al.*, 1995, 2000; *Pike et al.*, 2001].

[31] Hysteresis loops measured to a maximum field of 1 T from 89 sediment samples were included in the unmixing procedure. The measured hysteresis loops have a high signal-to-noise ratio with a mean Q value of 5.6 [cf. *Jackson and Solheid*, 2010]. The loops were processed using the method discussed in section 2 and formed into the data matrix, **X**. Eigenvector analysis reveals that the first 2 principal components of **X** explain ∼94% of the data variability, while the first 3 principal components explain ∼98%. As with the previous case study a more detailed model selection procedure was employed to select appropriate values of p and λ. For three end-members there is a clear break in C_{idx} at $\lambda \approx 0.33$, which demonstrates that one of the end-members has an increasingly large cross-over as the mixing simplex becomes larger (Figure 7). In contrast, I_{idx} has high values for all tested values of λ. The four end-member solutions have a similar break in C_{idx} at $\lambda \approx 0.1$, which occurs at a convexity error of approximately -2 compared to -3.3 for the position of the same break in the three end-member model. On this basis a three end-member model with $\lambda = 0.33$ is selected to represent the final mixing model. To demonstrate the quality of the final three end-member model the hysteresis loop with the largest fitting error is shown in Figure 8. Even for this worst case, the misfit between the hysteresis data and the end-member model is small with a root mean square error (RMSE) of ∼1.9×10^{-3} A m^2/kg.

[32] The unmixing model yields hysteresis loops that are consistent with the known magnetic mineralogy of the samples. End-member 1 is wasp-waisted and does not close until fields of ∼600 mT (Figure 9a), which is indicative of a mixture of high-coercivity and low-coercivity minerals, possibly with an additional zero-coercivity SP component [*Roberts et al.*, 1995; *Tauxe et al.*, 1996]. Given this composition, it is reasonable to assume that end-member 1
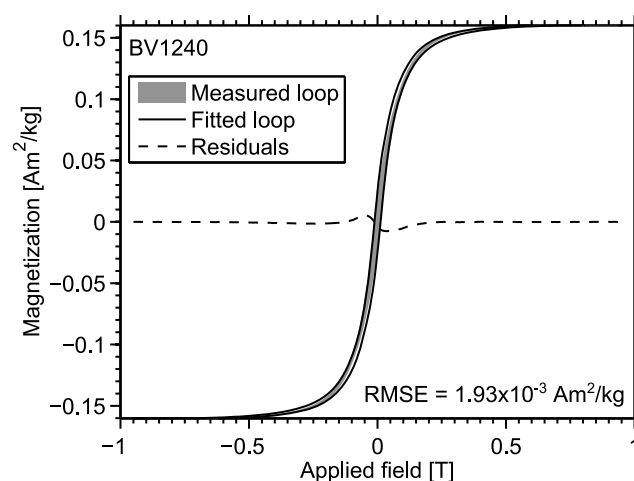
Figure 8. Butte Valley sample BV1240 yielded the largest mismatch between the measured data (gray shading) and the corresponding fit produced by the end-member model (solid line). The residuals, which were obtained by subtracting the end-member model fit from the data, indicate where the main mismatches occur.
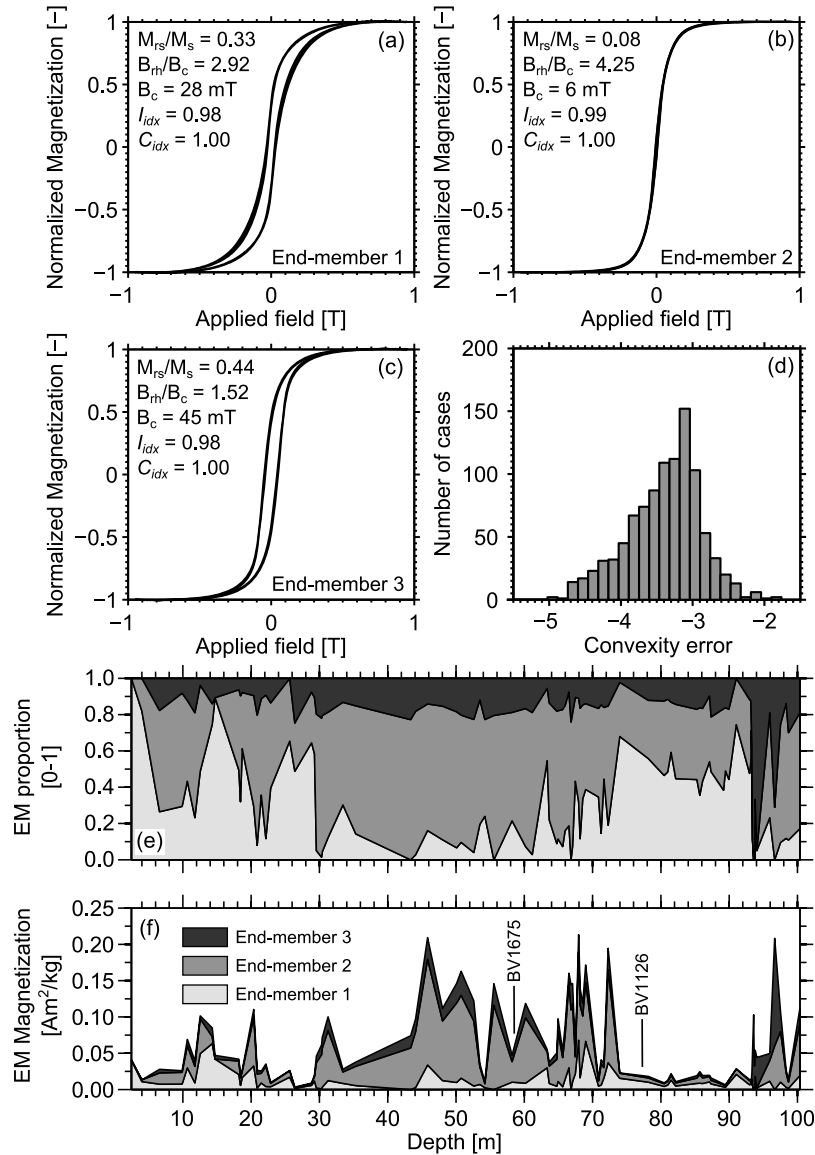
Figure 9. (a–c) The three end-members obtained by unmixing the Butte Valley hysteresis data. Each loop is shown as a shaded region indicating the mean loop ±1 standard error (estimated from the bootstrap procedure). Labels are as in Figure 6. (d) Histogram of the convexity errors produced by the 10^3 bootstrap iterations. (e) Relative and (f) absolute abundances of the three end-members for the Butte Valley data set as a function of depth. The positions of samples discussed in the text (BV1675 and BV1126) are marked.

corresponds to the mixed titanomagnetite and hematite mineralogy of the local detrital material originating from eroded catchment rocks [*Roberts et al.*, 1996]. End-member 2 has a magnetization that is almost completely reversible with a form that is indicative of SP or MD material (Figure 9b). FORC data from *Roberts et al.* [2000] and *Pike et al.* [2001] suggest that end-member 2 consists of SP rather than MD material. Additional evidence to support this designation is given below. Finally, end-member 3 has a SD form with a high M_{rs}/M_s value (Figure 9c). Given the form of end-member 3 it is interpreted as authigenic SD greigite with the possible addition of a small amount of SP greigite that lowers the M_{rs}/M_s ratio [*Roberts et al.*, 2011b]. Detailed justification of the interpretation of end-member 3

is given below. A histogram showing the distribution of convexity errors obtained for the 10^3 bootstrap iterations of the final end-member model is shown in Figure 9d.

[33] Mixing coefficients for the three end-members can be expressed as both relative proportions (Figure 9e) and absolute values (Figure 9f). Relative abundances, which sum to 1, are obtained directly from the mixing model as written in equation (5) and result from normalization of each hysteresis loop to $\hat{M} = 1$. These relative values can be converted into absolute values simply by multiplying the mixing proportions of a given sample by the measured value of $\hat{M}$. The end-member abundances and hysteresis loops are combined with existing rock magnetic data to aid environmental interpretation.
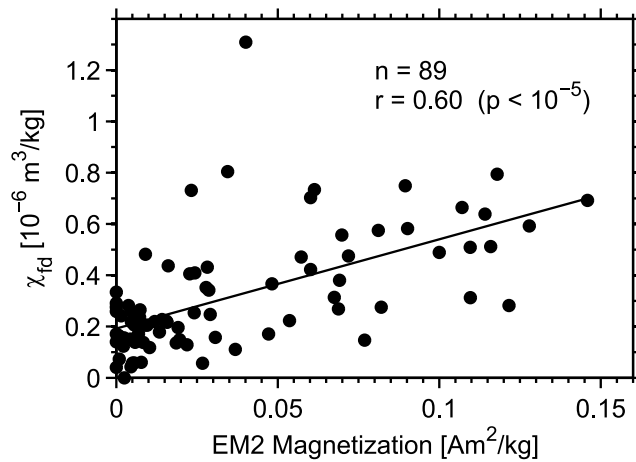
Figure 10. A significant correlation exists between the absolute magnetization of end-member 2 and χ_{fd}. Linear regression reveals a nonzero intercept, which indicates that one or both of the other end-members must also contain a small amount of SP material.

[34] Based on low-temperature analysis, *Roberts et al.* [1995] estimated that the magnetic mineral assemblage in sample BV1675 contained in excess of 80% SP material. FORC analysis of sample BV1126 revealed a secondary peak near the origin of the FORC diagram that is due to the presence of SP material; the FORC distribution also lacks vertical spreading that would be indicative of MD grains. The high relative abundance of end-member 2 in these samples (Figure 9e) confirms that the end-member corresponds to SP rather than to MD behavior. This conclusion is supported by comparison with the absolute frequency dependance of magnetic susceptibility, χ_{fd}, obtained from $\chi_{fd} = \chi_{lf} - \chi_{hf}$, where χ_{lf} and χ_{hf} are the magnetic susceptibilities at low (0.47 kHz) and high (4.7 kHz) frequencies, respectively. In a multiple linear regression model where the absolute end-member abundances act as the predictive terms and the response values are given by χ_{fd}, only the abundances of end-member 2 make a significant contribution to the regression model on the basis of a stepwise selection criterion at the 0.05 significance level [*Draper and Smith*, 1998]. Although this regression result should be treated with caution because of the presence of a weak multicollinearity between the absolute end-member abundances [*Swan and Sandilands*, 1995], the regression model adds support to the interpretation of end-member 2 as representing SP material (Figure 10). Identification of SP particles in the mixing model demonstrates one of the advantages of working with hysteresis data. Although the viscous fraction of SP/SSD material can have a detectable influence in IRM acquisition curves [*Heslop et al.*, 2004], it is difficult to detect by unmixing remanence data. In contrast, SP particles are detected readily by infield measurements and can be included in environmental magnetic interpretations using our hysteresis unmixing approach. An additional approach to identifying SP particles would be to remeasure the samples with a different field sweep rate and repeat the unmixing procedure to find how the form of the hypothesized SP end-member changed.

[35] The SD-type shape of end-member 3 suggests that it corresponds to authigenic greigite. To test if end-member 3 corresponds to a SD component, the end-member abundances are compared to M_{rs}/χ. It is important to note that because M_{rs}/χ is concentration independent, such a comparison must be based on relative rather than absolute end-member abundances. Samples were binned according to their M_{rs}/χ values and mean relative abundances of the end-members were determined for each bin (Figure 11). When end-member 2 is dominant, the M_{rs}/χ ratio is low because the M_{rs} value of SP particles is zero. For slightly higher M_{rs}/χ values, end-member 2 is gradually replaced by end-member 1 and M_{rs}/χ increases to values of ~3 kA m^{-1}. Finally, where end-member 3 is dominant, M_{rs}/χ values increase to their maximum of 5–8 kA m^{-1}, which in the Butte Valley sediments reflect the presence of SD greigite particles [*Roberts et al.*, 1996].

[36] The relative and absolute end-member abundances as a function of sediment depth (Figures 9e and 9f) reveal a pattern that aids interpretation of the end-member compositions. End-member 3 is the minor component throughout the core, except for an interval toward the base (~92–98 m) where it is dominant. Magnetic iron sulfides were identified in magnetic separates taken from this horizon [*Roberts et al.*, 1996] and had an appearance identical to fine-grained greigite from the Simpson oil field, Alaska [*Reynolds et al.*, 1994]. Given the SD form of the end-member and its association with high M_{rs}/χ values, it clearly corresponds to SD greigite. Finally, end-member 2 is the dominant component throughout the sedimentary sequence. Our analysis indicates that end-member 2 is almost entirely composed of SP material. Support for the presence of a detrital SP component is given by *Reynolds et al.* [2004] and *Rosenbaum and Reynolds* [2004a, 2004b], who studied lake sediments from the same Klamath Basin catchment as the Butte Valley
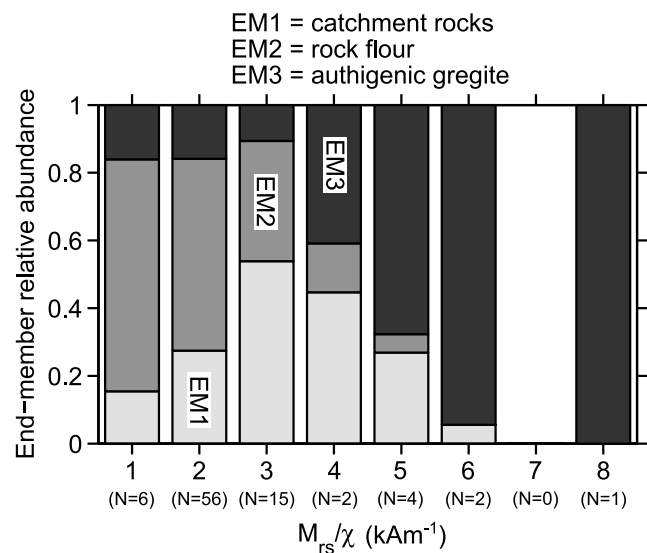
Figure 11. Relationship between the relative end-member abundances and M_{rs}/χ (an indicator of the relative abundance of SD grains). Samples were binned according to their M_{rs}/χ values, and the mean end-member relative abundances were calculated for each bin. The number of samples in each bin are shown (note the bin centered on 7 kA m^{-1} is empty).

sediments. *Reynolds et al.* [2004] identified two detrital components in sediments from Upper Klamath Lake, Oregon, that correspond to different weathering and transport regimes. The first component comprised volcanic clasts containing weathered titanomagnetite, which resulted in hematite production by oxidation. A similar detrital component composed of titanomagnetite and hematite was also observed at nearby Buck lake, southern Oregon [*Rosenbaum et al.*, 1996]. This combination of low- and high-coercivity detrital minerals is consistent with the wasp-waisted form of end-member 1. The second detrital component was interpreted to represent rock flour produced by glacial action that contains extremely fine-grained magnetic particles with SP characteristics [*Rosenbaum and Reynolds*, 2004a, 2004b]. The magnetic mineral assemblage of such a rock flour component is consistent with end-member 2.

[37] We have demonstrated that the presented hysteresis unmixing method provides a meaningful representation of the Butte Valley hysteresis data. The isolated end-members can be identified and associated with processes that are known to control the magnetic mineral assemblage of the studied samples. Our analysis unlocks a quantitative interpretation of the respective magnetic mineral components in the studied Butte Valley core. The ability to determine stratigraphic variations of magnetic components from hysteresis data has considerable potential in quantitative environmental magnetism.

5. Discussion and Conclusions

[38] We have presented a new unmixing method for decomposing hysteresis data into a collection of end-members under an assumption of linear mixing. The method is based on a modeling approach that focuses on covariation within a collection of hysteresis loops. In this way, limited assumptions concerning shape of the loops are made and there is no requirement to select from arbitrary basis functions that are thought to approximate the form of naturally occurring hysteresis loops. Through use of soft constraints, estimation of the mixing model is robust to outliers and is therefore not unduly affected by small numbers of samples with magnetic particles that do not originate from the mixing system (e.g., an exogenous ash layer in a sediment sequence).

[39] The quality of a final mixing model will depend heavily on the quality of the data from which it was constructed. We therefore recommend that measured loops are preprocessed using protocols such as those of *Jackson and Solheid* [2010] to ensure a high-quality input. It is essential for the user to consider the feasibility that magnetic mineral assemblages under investigation resulted from persistent geological environmental mixing. If this assumption is not reasonable, inappropriate application of an end-member unmixing method will produce spurious results. It is also important to remember that the abundances of high-coercivity minerals that are not saturated fully during a hysteresis experiment will be underrepresented in the mixing model compared to their real abundance in the magnetic mineral assemblage.

[40] The key aim of this work has been to enable quantitative analysis of hysteresis data with a focus on characterization of processes that control the composition of a magnetic mineral assemblage. As with other unmixing techniques, for example, those applied to decomposition of IRM acquisition curves, the components of the mixing model require detailed classification before they can be meaningfully interpreted. Therefore, unmixing cannot be applied in isolation. An additional suite of rock magnetic data is usually needed to help characterize the components, therefore the unmixing results will only form part of an overall interpretational framework for a data set. Nevertheless, the proposed unmixing method can help to unlock quantitative environmental magnetic interpretations.

Appendix A: Convexity Error

[41] To assess the extent to which a set of observations is bound by a simplex we employ a convexity error, which measures the difference between S and an ideal model that bounds all observations [*Weltje*, 1997]. In this way, the convexity error is a measure of misfit between the unmixing model and the data. The convexity error is given by

$$\log_{10}(P) + \log_{10}(D), \tag{A1}$$

where P is the proportion of observations located outside the simplex defined by S and D is their mean squared distance to the simplex. Therefore, low convexity errors are indicative of mixing models that are close to bounding all of the observations.

References

Barron, J. A., J. G. Baldauf, E. Barrera, J.-P. Caulet, B. T. Huber, B. H. Keating, D. Lazarus, H. Sakai, H. R. Thierstein, and W. Wei (1991), Biochronologic and magnetochronologic synthesis of Leg 119 sediments from the Kerguelen Plateau and Prydz Bay, Antarctica, *Proc. Ocean Drill. Proj. Sci. Results*, *119*, 813–847.

Bioucas-Dias, J. (2009), A variable splitting augmented Lagrangian approach to linear spectral unmixing, in *Hyperspectral Image and Signal Processing: Evolution in Remote Sensing, 2009. WHISPERS'09*, pp. 1–4, Inst. of Electr. and Electron. Eng., Piscataway, N. J., doi:10.1109/WHISPERS.2009.5289072.

Bowen, G. J., D. J. Beerling, P. L. Koch, J. C. Zachos, and T. Quattlebaum (2004), A humid climate state during the Palaeocene/Eocene thermal maximum, *Nature*, *432*, 495–499.

Carter-Stiglitz, B., B. Moskowitz, and M. Jackson (2001), Unmixing magnetic assemblages and the magnetic behavior of bimodal mixtures, *J. Geophys. Res.*, *106*, 26,397–26,411.

Carvallo, C., A. R. Muxworthy, and D. J. Dunlop (2006), First-order reversal curve (FORC) diagrams of magnetic mixtures: Micromagnetic models and measurements, *Phys. Earth Planet. Inter.*, *154*, 308–322.

Chan, T.-H., C.-Y. Chi, Y.-M. Huang, and W.-K. Ma (2009), A convex analysis-based minimum-volume enclosing simplex algorithm for hyperspectral unmixes, *IEEE Trans. Signal Processes*, *57*, 4418–4432.

Craig, M. (1994), Minimum-volume transforms for remotely sensed data, *IEEE Trans. Geosci. Remote Sens.*, *32*, 542–552, doi:10.1109/36.297973.

Diester-Haass, L. (1991), Eocene/Oligocene paleoceanography in the Antarctic Ocean, Atlantic sector (Maud Rise, ODP Leg 113, Site 689B and 690B), *Mar. Geol.*, *100*, 249–276.

Draper, N. R., and H. Smith (1998), *Applied Regression Analysis*, Wiley-Intersci., Hoboken, N. J.

Dunlop, D. J. (2002), Theory and application of the Day plot (M_{rs}/M_s versus H_{cr}/H_c): 1. Theoretical curves and tests using titanomagnetite data, *J. Geophys. Res.*, *107*(B3), 2056, doi:10.1029/2001JB000486.

Dunlop, D. J., and B. Carter-Stiglitz (2006), Day plots of mixtures of superparamagnetic, single-domain, pseudosingle-domain, and multidomain magnetites, *J. Geophys. Res.*, *111*, B12S09, doi:10.1029/2006JB004499.

Egli, R. (2003), Analysis of the field dependence of remanent magnetization curves, *J. Geophys. Res.*, *108*(B2), 2081, doi:10.1029/2002JB002023.

Egli, R. (2004a), Characterization of individual rock magnetic components by analysis of remanence curves. 1. Unmixing natural sediments, *Stud. Geophys. Geod.*, *48*, 391–446.

Egli, R. (2004b), Characterization of individual rock magnetic components by analysis of remanence curves. 2. Fundamental properties of coercivity distributions, *Phys. Chem. Earth*, *29*, 851–867, doi:10.1016/j.pce.2004.04.001.

Ehrlich, R., and W. E. Full (1987), Sorting out geology—Unmixing mixtures, in *Use and Abuse of Statistical Methods in the Earth Sciences*, *Stud. Math. Geol.*, vol. 1, pp. 33–46, Oxford Univ. Press, New York.

Evans, M. E., and F. Heller (2003), *Environmental Magnetism: Principles and Applications of Enviromagnetics*, *Int. Geophys. Ser.*, vol. 86, Academic, Amsterdam.

Fabian, K. (2006), Approach to saturation analysis of hysteresis measurements in rock magnetism and evidence for stress dominated magnetic anisotropy in yound mid-ocean ridge basalt, *Phys. Earth Planet. Inter.*, *154*, 299–307.

Fabian, K., and T. von Dobeneck (1997), Isothermal magnetization of samples with stable Preisach function: A survey of hysteresis, remanence, and rock magnetic parameters, *J. Geophys. Res.*, *102*, 17,659–17,677, doi:10.1029/97JB01051.

Florindo, F., and A. P. Roberts (2005), Eocene-Oligocene magnetobiochronology of ODP Sites 689 and 690, Maud Rise, Weddell Sea, Antarctica, *Geol. Soc. Am. Bull.*, *117*, 46–66.

Harding, I. C., et al. (2011), Sea-level and salinity fluctuations during the Paleocene–Eocene thermal maximum in Arctic Spitsbergen, *Earth Planet. Sci. Lett.*, *303*, 97–107, doi:10.1016/j.epsl.2010.12.043.

Heslop, D. (2005), A Monte Carlo investigation of the representation of thermally activated single-domain particles within the Day plot, *Stud. Geophys. Geod.*, *49*, 163–176.

Heslop, D., and M. Dillon (2007), Unmixing magnetic remanence curves without a priori knowledge, *Geophys. J. Int.*, *170*, 556–566, doi:10.1111/j.1365-246X.2007.03432.x.

Heslop, D., M. J. Dekkers, P. P. Kruiver, and I. H. M. van Oorschot (2002), Analysis of isothermal remanent magnetization acquisition curves using the expectation-maximization algorithm, *Geophys. J. Int.*, *148*, 58–64.

Heslop, D., G. McIntosh, and M. Dekkers (2004), Using time and temperature dependant Preisach models to investigate the limitations of modelling isothermal remanent magnetisation curves with cumulative log Gaussian functions, *Geophys. J. Int.*, *157*, 55–63.

Hesse, P. P. (1994), Evidence for bacterial palaeoecological origin of mineral magnetic cycles in oxic and sub-oxic Tasman Sea Sediments, *Mar. Geol.*, *117*, 1–17.

Imbrie, J. (1963), Factor and vector analysis programs for analyzing geologic data, *Tech. Rep. 6*, Geogr. Branch, Off. of Nav. Res., Washington, D. C.

Jackson, M., and P. Solheid (2010), On the quantitative analysis and evaluation of magnetic hysteresis data, *Geochem. Geophys. Geosyst.*, *11*, Q04Z15, doi:10.1029/2009GC002932.

Kahaner, D., C. Moler, and S. Nash (1989), *Numerical Methods and Software*, Prentice-Hall, Englewood Cliffs, N. J.

Kennett, J. P., and P. F. Barker (1990), Latest Cretaceous to Cenozoic climate and oceanographic developments in the Weddell Sea, Antarctica: An ocean drilling perspective, *Proc. Ocean Drill. Program Sci. Results*, *113*, 937–960.

Kruiver, P. P., M. J. Dekkers, and D. Heslop (2001), Quantification of magnetic coercivity components by the analysis of acquisition curves of isothermal remanent magnetisation, *Phys. Earth Planet. Inter.*, *189*, 269–276.

Lanci, L., and D. V. Kent (2003), Introduction of thermal activation in forward modeling of hysteresis loops for single-domain magnetic particles and implications for the interpretation of the Day diagram, *J. Geophys. Res.*, *108*(B3), 2142, doi:10.1029/2001JB000944.

Lascu, I., S. K. Banerjee, and T. S. Berquó (2010), Quantifying the concentration of ferrimagnetic particles in sediments using rock magnetic methods, *Geochem. Geophys. Geosyst.*, *11*, Q08Z19, doi:10.1029/2010GC003182.

Lees, J. A. (1997), Mineral magnetic properties of mixtures of environmental and synthetic materials: Linear additivity and interaction effects, *Geophys. J. Int.*, *131*, 335–346.

Marques de Sá, J. P. (2007), *Applied Statistics Using SPSS, STATISTICA, MATLAB and R*, 2nd ed., Springer, Berlin.

Miao, L., and H. Qi (2007), Endmember extraction from highly mixed data using minimum volume constrained nonnegative matrix factorization, *IEEE Trans. Geosci. Remote Sens.*, *45*, 765–777, doi:10.1109/TGRS.2006.888466.

Pagani, M., N. Pedentchouk, M. Huber, A. Sluijs, S. Schouten, H. Brinkhuis, J. S. Sinninghe Damsté, G. R. Dickens, and the Expedition 302 Scientists (2006), Arctic hydrology during global warming at the Palaeocene/Eocene thermal maximum, *Nature*, *442*, 671–675, doi:10.1038/nature05043.

Pike, C. R., A. P. Roberts, and K. L. Verosub (2001), First-order reversal curve diagrams and thermal relaxation effects in magnetic particles, *Geophys. J. Int.*, *145*, 721–730, doi:10.1046/j.0956-540x.2001.01419.x.

Renner, R. (1995), The construction of extreme compositions, *Math. Geol.*, *27*, 485–497, doi:10.1007/BF02084423.

Reynolds, R. L., M. L. Tuttle, C. A. Rice, N. S. Fishman, J. A. Karachewski, and D. M. Sherman (1994), Magnetization and geochemistry of greigite-bearing Cretaceous strata, North Slope Basin, Alaska, *Am. J. Sci.*, *294*, 485–528.

Reynolds, R. L., J. G. Rosenbaum, J. Rapp, M. W. Kerwin, J. P. Bradbury, S. Colman, and D. Adam (2004), Record of late Pleistocene glaciation and deglaciation in the southern Cascade Range. I. Petrological evidence from lacustrine sediment in Upper Klamath Lake, southern Oregon, *J. Paleolimnol.*, *31*, 217–233.

Rivas, J., J. M. Zamarro, E. Martin, and C. Pereira (1981), Simple approximation for magnetization curves and hysteresis loops, *IEEE Trans. Magn.*, *17*, 1498–1502, doi:10.1109/TMG.1981.1061241.

Roberts, A. P., Y. Cui, and K. L. Verosub (1995), Wasp-waisted hysteresis loops: Mineral magnetic characteristics and discrimination of components in mixed magnetic systems, *J. Geophys. Res.*, *100*, 17,909–17,924, doi:10.1029/95JB00672.

Roberts, A. P., R. L. Reynolds, K. L. Verosub, and D. P. Adam (1996), Environmental magnetic implications of greigite (Fe_3S_4) formation in a 3 m.y. lake sediment record from Butte Valley, northern California, *Geophys. Res. Lett.*, *23*, 2859–2862.

Roberts, A. P., C. R. Pike, and K. L. Verosub (2000), First-order reversal curve diagrams: A new tool for characterizing the magnetic properties of natural samples, *J. Geophys. Res.*, *105*, 28,461–28,475.

Roberts, A. P., F. Florindo, G. Villa, L. Chang, L. Jovane, S. M. Bohaty, J. C. Larrasoaña, D. Heslop, and J. D. Fitz Gerald (2011a), Magnetotactic bacterial abundance in pelagic marine environments is limited by organic carbon flux and availability of dissolved iron, *Earth Planet. Sci. Lett.*, *310*, 441–452.

Roberts, A. P., L. Chang, C. J. Rowan, C.-S. Horng, and F. Florindo (2011b), Magnetic characteristics of sedimentary greigite (Fe_3S_4): An update, *Rev. Geophys.*, *49*, RG1002, doi:10.1029/2010RG000336.

Robertson, D. J., and D. E. France (1994), Discrimination of remanence carrying minerals in mixtures, using isothermal remanent magnetization aquisition curves, *Phys. Earth Planet. Inter.*, *82*, 223–234.

Rosenbaum, J. G., and R. L. Reynolds (2004a), Record of late Pleistocene glaciation and deglaciation in the southern Cascade Range. II. Flux of glacial flour in a sediment core from Upper Klamath Lake, Oregon, *J. Paleolimnol.*, *31*, 235–252.

Rosenbaum, J. G., and R. L. Reynolds (2004b), Basis for paleoenvironmental interpretation of magnetic properties of sediment from Upper Klamath Lake (Oregon): Effects of weathering and mineralogical sorting, *J. Paleolimnol.*, *31*, 253–265.

Rosenbaum, J. G., R. L. Reynolds, D. P. Adam, J. Drexler, A. M. Sarna-Wojcicki, and G. C. Whitney (1996), Record of middle Pleistocene climate change from Buck Lake, Cascade Range, southern Oregon—Evidence from sediment magnetism, trace-element geochemistry, and pollen, *Geol. Soc. Am. Bull.*, *108*, 1328–1341.

Stockhausen, H. (1998), Some new aspects for the modelling of isothermal remanent magnetization acquisition curves by cumulative log Gaussian functions, *Geophys. Res. Lett.*, *25*, 2217–2220.

Swan, A. R. H., and M. Sandilands (1995), *Introduction to Geological Data Analysis*, Blackwell Sci., Oxford, U. K.

Tauxe, L., T. A. T. Mullender, and T. Pick (1996), Potbellies, wasp-waists, and superparamagnetism in magnetic hysteresis, *J. Geophys. Res.*, *101*, 571–583.

Thompson, R. (1986), Modelling magnetization data using SIMPLEX, *Phys. Earth Planet. Inter.*, *42*, 113–127.

von Dobeneck, T. (1996), A systematic analysis of natural magnetic mineral assemblages based on modelling hysteresis loops with coercivity-related hyperbolic basis functions, *Geophys. J. Int.*, *124*, 675–694, doi:10.1111/j.1365-246X.1996.tb05632.x.

Weltje, G. J. (1997), End-member modeling of compositional data: Numerical-statistical algorithms for solving the explicit mixing problem, *Math. Geol.*, *29*, 503–549.

D. Heslop and A. P. Roberts, Research School of Earth Sciences, Australian National University, Canberra ACT 0200, Australia. (david.heslop@anu.edu.au)